Enhanced Object Localization using Side Lobes of Antenna Pattern in mmWave Beamforming ISAC System

Ekaterina Sedunova[1,2]
[1] IHP – Leibniz-Institut für innovative Mikroelektronik
Frankfurt Oder, Germany
[2] Computer Science department
Humboldt University of Berlin
Berlin, Germany
sedunova@ihp-microelectonics.de

Markus Petri[1]
[1] IHP – Leibniz-Institut für innovative Mikroelektronik
Frankfurt Oder, Germany
petri@ihp-microelectronics.de

Eckhard Grass[1,2]
[1] IHP – Leibniz-Institut für innovative Mikroelektronik
Frankfurt Oder, Germany
[2] Computer Science department
Humboldt University of Berlin
Berlin, Germany
grass@ihp-microelectronics.de

***Abstract*—This work is focused on enhancing the object localization and room reconstruction using an Integrating Sensing and Communication (ISAC) system in the millimeter-wave range. The applications of ISAC can improve the generation or accuracy of digital twins and assist in fast switching between steering vectors for robust communication. In this paper, we utilized the antenna pattern knowledge to scan objects in the areas that are not covered by intersections of the main lobe beams. We also utilize the side lobe and main lobe intersection. In order to evaluate the suggested approach, we created two different room models with the transmitter and the receiver located apart from each other – similar to a bistatic RADAR set-up. Both nodes are equipped with phased array antennas that perform beam steering. The digitized beam patterns are used for all simulations. The propagated signal over channel is obtained via ray-tracing simulations and cross-correlated to obtain the channel impulse response (CIR). Based on the CIR, we applied the LASSO technique. The obtained results are visualized and evaluated. This paper presents the approach of extending the sensing area for object localization from the main intersection of the beam steering angles to the side and main lobe intersection area using the complete antenna patterns, including the side lobes.**

Keywords— ISAC, mmWave, localization, sensing, antenna pattern, 6G, joint communication and sensing (JCAS)

1. Introduction

Since the origin of wireless communications using electromagnetic waves, wireless technologies have experienced continuously increasing performance requirements across various applications. Early generations of wireless networks primarily focused on reliable voice transmission for phone calls. However, with the advent of smartphones, data transmission has grown exponentially and become the top priority for the third and fourth generations of mobile communications [1]. The continuous growth in the number of connected devices has placed significant strain on the available radio frequency spectrum, which is increasingly insufficient to meet user demands. The average household currently has more than five devices that are connected to the wireless network: from the personal computer and mobile phone to the vacuum cleaner and even electric kettle [2]. To overcome the limitation of the spectrum, we see the potential of millimeter-wave (mmWave) systems for significantly increasing channel bandwidth and network capacity [3]. The advantages of using the mmWave frequency range would be not only the increased capacity, but also new applications for sensing [4]. This, in turn, can help provide better coverage and faster beam switching. Beamforming is a necessary technique to mitigate the high path loss for mmWave carrier frequencies. While the high path loss can be compensated with phased array antennas, it also enables reduced interference in multi-user environments. By leveraging beamforming techniques and directional signal transmission, mmWave communication can effectively concentrate electromagnetic energy toward the intended receiver, thereby enhancing link reliability and spectral efficiency [5].

Since blockages of the Line-of-Sight (LoS) path can significantly deteriorate the communication link, adaptive beamforming techniques are being widely investigated [6], [7]. One possible solution to support rapid beam switching would be algorithms based on the knowledge of the environment in which the communication nodes are located. This is one reason Integrated Sensing and Communication (ISAC) systems are receiving more scientific attention and are considered a key technology for 6G mobile communications [8]. Object localization can be part of some room reconstruction and could also be used to create or enrich a digital twin of the indoor environment. A digital twin, in turn, would allow efficient prediction of the system behavior based on the surroundings and, most significantly, actors participating in the scenario [9]. In this way, fast and proactive reactions to dynamically changing environments and propagation characteristics are facilitated.

Phased array antennas are being widely used for beamforming. The standard practice is to define the amplitude-phase weights for each antenna element to create a codebook where the antenna patterns are pre-specified, typically focusing on the main lobe directions. A rectangular antenna array typically allows good steering capabilities in a maximum angular range from ca. – 60° to 60° for the main beam. However, the width of the main lobe increases with steering vectors approaching +/-90 degree. Introducing our approach, we utilize the knowledge of the antenna pattern, including the side lobes, to increase the area of the room that can be scanned.

The authors acknowledge the financial support by the German Federal Ministry of Research, Technology and Space (BMFTR) within the project Open6GHub under grant reference number 16KISK009.

The main contribution of this paper is a new approach to increase the scan area for object localization utilizing the complete antenna patterns. The results are shown for two slightly different simulated environments. To obtain the CIRs for different beams of the codebook, ray-tracing simulations with digitized antenna patterns are performed. Our study proves that the combined gain of the main and side lobes of multiple antenna patterns provides sufficient information to detect potential objects in an extended scan range. Furthermore, the detection accuracy in the main lobe intersection area is improved due to re-allocation of the power towards true reflections or diffraction points.

This paper is organized as follows: After the Introduction, Section II describes the system model, the mathematical concept, as well as the limitations and assumptions presented throughout the paper. Our suggested approach for the object localization is presented in Section III and results are shown in Section IV which is followed by Conclusions with an outlook on future work in Section V.

2. System Model

2.1 Scenario

In this study, we consider an indoor scenario with one transmitter (Tx) and one receiver (Rx) located apart, resembling a bi-static scenario for RADARs. Both nodes (antenna arrays) are oriented towards each other, so that at least one combination of steering vectors highlights the LoS path. In order to showcase the suggested method in a simple and structured way, we omit the elevation axis and search only for the objects in the azimuth direction. Therefore, both devices are located on the same plane. The method can be adjusted for three dimensions. However, this would significantly increase the computational complexity for processing the measurement and/or simulation data.

The main beam of the transmitter and the receiver can be steered using phased array antennas. In this scenario, a uniform rectangular array (URA) consisting of 16 elements along the horizontal and 2 along the vertical axis, forms the 16 × 2 patch array structure. The element spacing of the URA is λ/2, where $\lambda = \frac{c}{f_c}$, λ – wavelength, f_c is carrier frequency, in our case 60 GHz, and c is the speed of the electromagnetic waves in vacuum (299,792,458 m/s). Thus, the distance between two patch elements is approximately equal to 2.498 mm. The array geometry and 3D antenna pattern of an individual patch element are presented in Fig. 1 and 2, respectively. In case of beamforming with URA, beams that are getting closer to ±90° become wider and increasingly indistinguishable from each other in the angular space (Fig. 3).

To achieve a relatively small beam width in the antenna patterns, we limit the beamforming range from -46.5° to 46.5°. Therefore, the codebook consists of 63 antenna patterns with a step size of 1.5°. The angular resolution of each discretized and digitized antenna pattern has an impact on the resolution of the final point cloud grid, which in turn determines the potential precision of the object localization. For the current simulation setup, the angular resolution of the discretized antenna patterns was chosen as 1° in the azimuth plane, in the range of -90° to 90°, since we assume no radiation or sensitivity of the antennas in the backward direction for the both devices.

The chosen parameters correspond to the real capabilities of the available transceivers, for example, as used in [10]. Figure 4 shows a few antenna patterns from the codebook for -39°, -21°, 0°, 12°, 30°, and 45° steering vectors. As shown, the maximum gain of the main lobe can almost reach 20 dB, and side lobes can reach nearly 10 dB gain. There are visible notches for certain azimuth angles θ for each individual antenna pattern. To better visualize the spatial characteristics of the beam steering antenna, a 3D radiation pattern for 0° is shown in the Fig. 5. Nevertheless, a complete angular range from -90° to 90° can be covered either by intersections of the transmitter and receiver main lobes or by combinations of one main lobe and one side lobe from any of the communication nodes, provided that the total received power per ray exceeds the noise level.

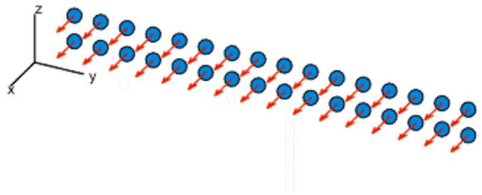

Fig. 1. Geometry of the uniform rectangular antenna array

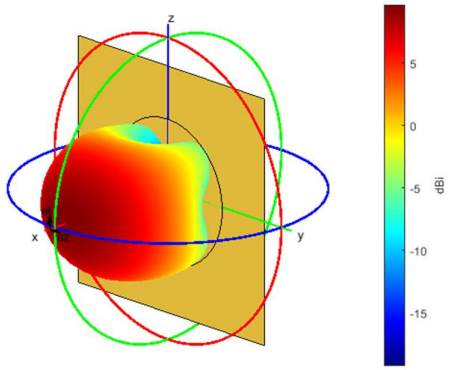

Fig. 2. 3D Radiation pattern of the individual patch element

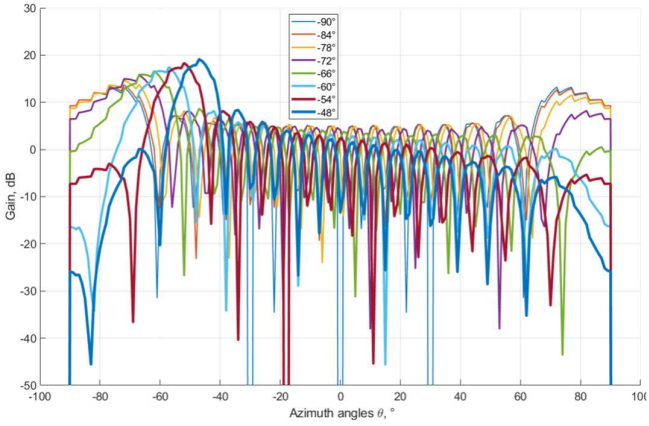

Fig. 3. Example of the beam pattern for steering vectors from -90° to -48° where main lobe distortion presents difficulties for identifying the received power that would belong to certain angles.

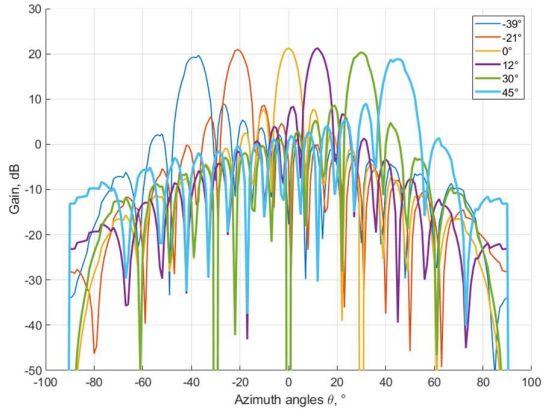

Fig. 4. Example of the directivity of antenna patterns from the generated code book based on the 16 × 2 URA patch elements for 60 GHz carrier frequency with 2.498 mm element spacing.

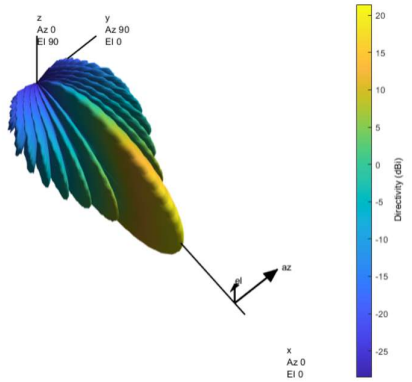

Fig. 5. 3D radiation pattern for the array antenna with steering vector 0°

2.2 Channel Model, Ray-Tracing Model and room environment

The wireless channel in the millimeter-wave range is typically sparse. Therefore, it can be accurately simulated with a deterministic ray-tracing (RT) model that utilizes the geometry of the environment, hence, captures the physical objects through the interactions of the electromagnetic waves, including reflections and diffractions. Our simulations are performed using the MATLAB Antenna and Phased Array Antenna System toolboxes [11], [12], where scattering effects are not directly supported. To evaluate whether the method is still applicable for objects having multiple reflections similar to scattering, we created an STL file where object surfaces are represented as sharp-edge triangles combined together. We assume only first-order diffraction. From the ray-tracing (RT) model's point of view, it is only possible to sense objects that interact with the propagated rays through reflection or diffraction. As a result, only valid rays that reach the receiver contribute to the channel impulse response, which is ultimately the result of all received rays. All objects that do not cause reflections or diffractions after running the ray-tracer, will not play any role in the channel impulse response (CIR) generation. To test the different behavior resulting from this limitation, we applied the method to two slightly different environments. For the first one, only first-order reflection and diffraction are incorporated, whereby most of the objects are presented with relatively flat surfaces

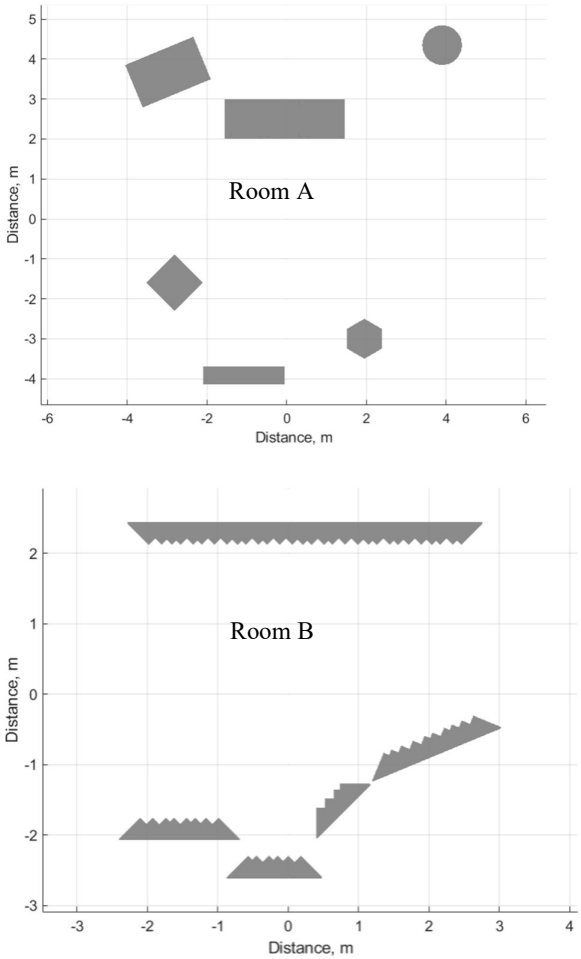

Fig. 6. Room A with relatively flat surfaces and Room B with sharp edges, top view

The second scenario uses the "sharp-edge" surfaces with only the diffraction effect (see Fig. 6, Room A and Room B). The purpose of this second scenario is to explicitly model penetration- and roughness induced scattering rather than specular reflection alone.

By propagating the signal from transmitter (Tx) to the receiver (Rx) though the wireless channel, we can describe the received signal *y(t)* as a convolution of the propagated signal *x(t)* and the channel impulse response *h(t)* combined with additive white Gaussian noise *n(t)* at the receiver side:

$$y(t) = h(t) * x(t) + n(t). \quad (1)$$

The transmitted signal $x(t)$ is constructed from four consecutive repetitions of a Zadoff-Chu (ZC) sequence [13], which is widely used in wireless communication systems due to its excellent autocorrelation properties and constant amplitude. Each ZC sequence has a length of 1023 samples, and is generated with a root index of 53, ensuring a good balance between sequence complexity and correlation performance. Using the cross-correlation ⊗ between the received signal and a single Zadoff-Chu sequence, we calculate the channel impulse response:

$$\hat{h}(t) = y(t) \otimes x(t). \quad (2)$$

The first and last sequences might be corrupted by different factors and in particular filtering (Fig. 7). Therefore, we perform the averaging over the two middle ZC sequences to reduce the influence of noise.

In order to obtain a full dataset, beamforming over the complete codebook, for both for the transmitter and receiver main steering vectors, ψ_{Tx} and φ_{Rx} correspondingly, is modelled:

$$y(t, \psi_{Tx}, \varphi_{Rx}) = h(t, \psi_{Tx}, \varphi_{Rx}) * x(t) + n(t), \quad (3)$$

Furthermore, the received power at a single time instance τ is recorded as the superposition of all relevant rays of the digitized antenna pattern:

$$h(\tau, \psi_{Tx}, \varphi_{Rx}) = \sum_{k=1}^{K} r_k(\alpha_k, \beta_k, \tau) \cdot G_{tot}(\psi_{Tx}, \alpha_k, \varphi_{Rx}, \beta_k), \quad (4)$$

where the $r_k(\alpha_k, \beta_k, \tau) = P_k(\tau) \cdot R_k$ is the ray represented by the path loss P_k and its reflectivity R_k of the point that is created by interaction between the given ray k that reached the receiver at time moment τ and room environment. Parameters α_k and β_k denote Angle of Departure (AoD) and Angle of Arrival (AoA) for each path $k \in \{1, 2 \dots K\}$, respectively.

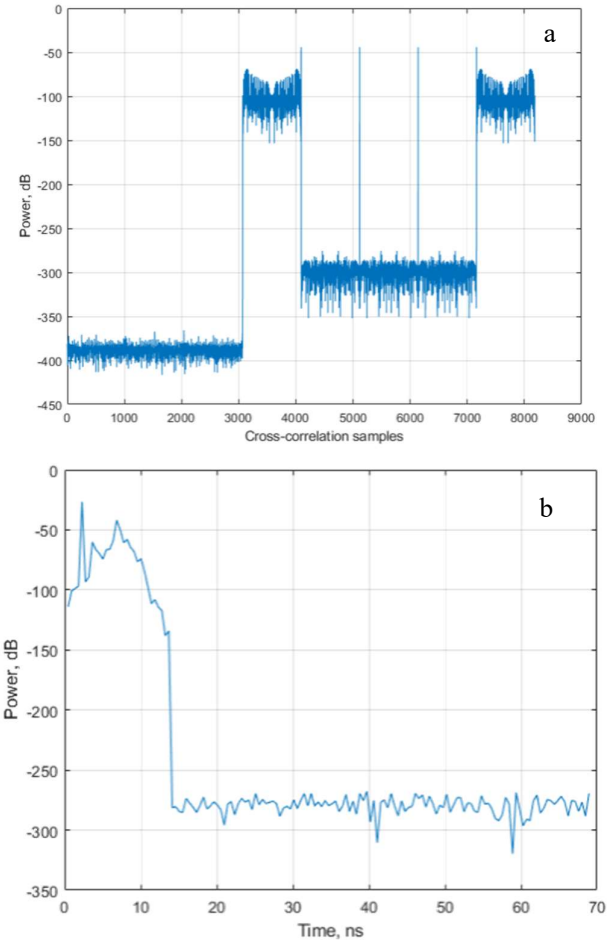

Fig. 7. Example of (a) Cross-correlation between the transmitted waveform and a single Zadoff-Chu Sequence for the Line-of-Sight transmission only, and (b) Power delay profile for the multipath propagation scenario for an arbitrarily chosen pair of Tx and Rx steering vectors without added noise to the received signal.

Antenna gains of the transmitter $G_{Tx}(\psi_{Tx}, \alpha_k)$ and receiver $G_{Rx}(\varphi_{Rx}, \alpha_k)$ are associated with the paths where reflections can potentially occur. The total gain G_{tot} for both transmitter and receiver antennas for individual AoA and AoD combinations corresponding to the steering vectors can be written as:

$$G_{tot}(\psi_{Tx}, \alpha_k, \varphi_{Rx}, \beta_k) = G_{Tx}(\psi_{Tx}, \alpha_k) \cdot G_{Rx}(\varphi_{Rx}, \beta_k). \quad (5)$$

III Object Localization using LASSO

3.1 Setup and pre-processing steps

In our previous studies [14], methods included finding the peak power for an intersection of a pair of steering vectors and interpreting this peak as the reflectivity of a potential object at this intersection. Antenna pattern deconvolution methods, applied to the resulting power map, helped to reduce the effect of the side lobe influence on the power map [15]. In cases, when it is possible to use mechanical steering of antenna within the range of -90 ° to 90 ° and, with small beam width of the main beam, we could still cover most of the room and find the objects with good reflectivity properties. However, in [16], we limited the area for the main intersection points using the steering vectors from -45 ° to 45 ° range. As a result, the area where we could identify the objects was very limited, i.e. from -45 ° to 45 ° and did not provide a good coverage of the objects in the room. Additionally, we observed the effect of the transferring power from the side lobes to the area of intersections, which created false reflections (objects). De-convolution of changing antenna patterns, for eliminating the effect of side lobes, proved very difficult and was, therefore, not applied. The method outlined further below, allows using the energy transmitted and received via side lobes to be utilized for object detection.

Room A features a comparatively simple setup, whereas Room B is selected for general representation purposes. A power map (Fig. 8) helps to determine the pair of Tx-Rx angles for the LoS path, as well as shows the strong reflection points within the main intersection area of the beamforming angular Tx-Rx pairs. However, without postprocessing it is difficult to differentiate whether the peak in PDP is due to a side lobe or belongs to the reflection point associated with the pair of steering vectors. The main intersection area for Room B is shown in Fig. 9a. Notably, if one of the devices is rotated by 90°, the line-of-sight (LoS) path is lost, and the overall received power may no longer be sufficient to detect reflection peaks above the noise level. To address this limitation, we aim to incorporate knowledge of the antenna patterns, including their side lobe characteristics, to improve localization accuracy. The procedure for this approach is to an extend similar to the previous setup: the location of the transmitter and receiver are known relatively to each other (for example performing ranging procedure) and are used as the foci points of ellipses. The environment is separated into ellipses with the same step size as our sampling distance $d_{dist} = \frac{c}{f_s}$, where f_s is the sampling frequency. In our setups, f_s = 2.19 and f_s = 5 GHz are used, resulting in a sampling distance of 13.7 and 6 cm, respectively.

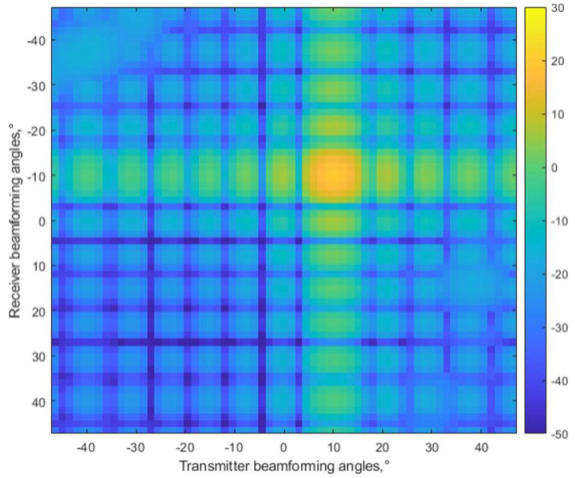

Fig. 8. Maximum power per pair of steering vectors, room B

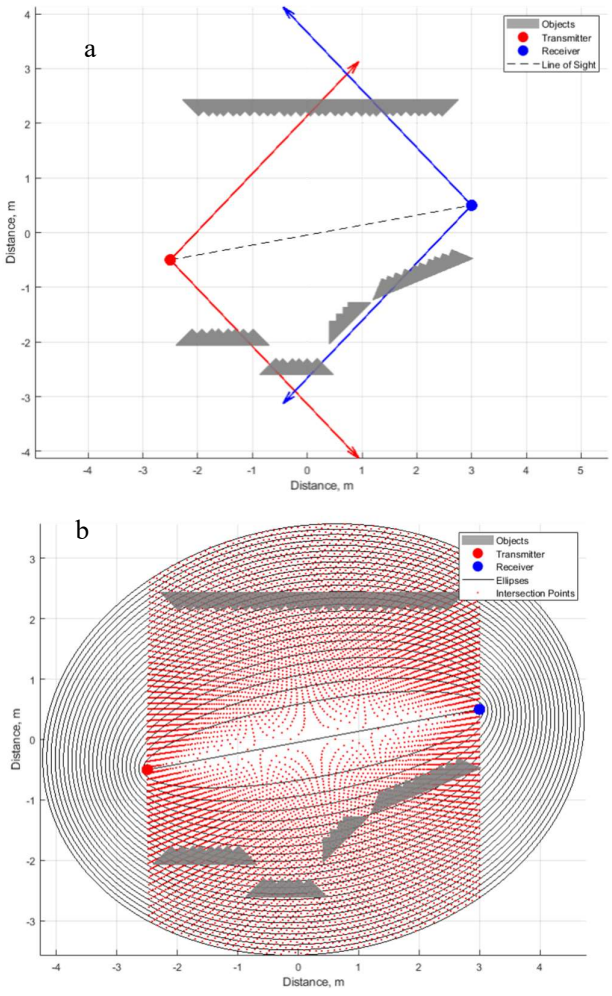

Fig. 9. (a) Example of the intersections area for Tx-Rx pairs for their main steering vectors (inside the room) and (b) Ellipses where foci points are Tx and Rx position with all possible points that intersect based on the resolution of the digitized antenna patterns

In the next step, the points generated by intersection rays from Tx and Rx within the angular resolution of angle d_θ (in our case 1° for both Tx and Rx) are calculated and assigned to areas between two consecutive ellipses that correspond to individual time instances in the power delay profile. Since no radiation or sensitivity from the back side of the antenna is considered, all possible points of intersections, i.e., reflectivity, in one plane are presented in Fig. 9b.

3.2 Solving the system of linear equations using LASSO

By performing a full sweep over all Tx and Rx steering vectors, we generate the power delay profiles for all combinations of steering vectors. Thereafter, a system of linear equations per each ellipse, in the classical matrix form $Ax = b$, is constructed, where A corresponds to the value $G_{tot}(\psi_{Tx}, \alpha_k, \varphi_{Rx}, \beta_k)$, x is the reflectivity of the point $R_p(\alpha_k, \beta_k)$ created by the intersection of rays from Tx with angle α_k and Rx at β_k and b is the power from the power delay profile for the steering vector $P(\psi_{Tx}, \varphi_{Rx})$ which results in:

$$\begin{cases} \sum_k^K G_{tot}\left(\psi_{Tx}^1, \alpha_k, \varphi_{Rx}^1, \beta_k\right) \cdot R_p\left(\alpha_k, \beta_k\right) = P\left(\psi_{Tx}^1, \varphi_{Rx}^1\right) \\ \sum_k^K G_{tot}\left(\psi_{Tx}^i, \alpha_k, \varphi_{Rx}^j, \beta_k\right) \cdot R_p\left(\alpha_k, \beta_k\right) = P\left(\psi_{Tx}^i, \varphi_{Rx}^j\right) \\ \sum_k^K G_{tot}\left(\psi_{Tx}^N, \alpha_k, \varphi_{Rx}^M, \beta_k\right) \cdot R_p\left(\alpha_k, \beta_k\right) = P\left(\psi_{Tx}^N, \varphi_{Rx}^M\right) \end{cases} \quad (6)$$

This system of equations cannot easily be solved using classical methods due to additive noise, uncertainty in the estimation of the power received from each ellipse, and the effects of filtering, which lead to high condition numbers in some of the matrices. This indicates high sensitivity of the results, making them unreliable. Since the number of points per each ellipse K can be significantly less than the combination of main steering vectors $N{\cdot}M$ and many R_p values are expected to be zero, linear regression methods can be used to fit all available data and attain reasonable results. In standard linear regression, the model estimates the coefficients by minimizing the sum of squared errors. However, when the number of predictors is large or when multicollinearity exists, the model can overfit the data [17]. Regularization methods introduce a penalty term to address this issue. One of the linear regression methods is LASSO (Least Absolute Shrinkage and Selection Operator) [18]. Its main purpose is to enhance prediction accuracy and interpretability by enforcing sparsity in the model coefficients. The LASSO method modifies the function by adding an L1 penalty term with a regularization parameter (RP) λ. Specifically, for our setup, the coefficients are estimated by minimizing the following expression:

$$r_p(\lambda) = \min_{r_p \epsilon R_p} \left(\left\| P - G_{tot} R_p \right\|_2^2 + \lambda \left\| r_p \right\|_1 \right). \quad (7)$$

3.3. Accuracy metrics

The RP λ was empirically chosen to minimize the estimators: Chamfer distance (CD) and Hausdorff distance (HD), which are common accuracy metrics for object localization. Chamfer distance can be used to estimate the average error between two point sets $A = \{a_1, a_2, \dots, a_m\}$ and $B = \{b_1, b_2, \dots, b_n\}$:

$$CD(A,B) = \frac{1}{|A|} \sum_{a \in A} \min_{b \in B} \|a - b\|_2^2 + \frac{1}{|B|} \sum_{b \in B} \min_{a \in A} \|b - a\|_2^2 . \quad (8)$$

On the other hand, the Hausdorff distance can be interpreted as 'worst-case scenario' for the estimation of the reflection points and is expressed as follows:

$$HD(A,B) = \max\left\{\max_{a\in A}\min_{b\in B}\|a-b\|, \max_{b\in B}\min_{a\in A}\|b-a\|\right\}. \quad (9)$$

The first point set is generated by identifying the reflection or diffraction points based on the interaction of the rays with objects in the Ray-Tracing model. We limit the rays to first-order reflections only. The second point set is created from non-zero r_p that passed the threshold 0.5 of the max value R_p received per ellipse. The optimal λ should be chosen with the aim to minimize both errors – the average and the furthest distance. It appears reasonable to introduce the 'coverage ratio' as an additional parameter for object localization, as it enables a more detailed assessment of reconstruction performance. Specifically, if we define estimated points as those lying within a distance threshold d_{dist} from their nearest ground truth points, the 'coverage ratio' quantifies the proportion of such points relative to the total number of ground truth points. This measure captures the extent to which the reconstructed data accurately represents the spatial distribution of the reference set. While regions with a high SNR generally provide accurate estimations, in areas with low SNR it is preferable to produce fewer reconstructed points (therefore, decrease the 'coverage ratio') rather than introducing false correspondences, as such points can degrade overall localization reliability.

In the simulation, it is straightforward to demonstrate that both metrics can achieve high precision within a certain area when all points are utilized. However, the HD-metrics can significantly worsen the final estimation in the case of a single outlier. Despite this, it is useful to see, what the longest distance between the actual reflection point and the estimation (i.e., the largest error) can be. Because both metrics ignore the geometry of the points, the final visualization can also be used to estimate the quality of the object localization.

IV. Visualization and Evaluation of the Results

We present the results for the two rooms A and B with two different sampling frequencies: 2.19 GHz and 5 GHz. For both rooms, the antenna pattern codebooks are the same: 63 steering vectors within an azimuth range -46.5° to 46.5° with a step size of 1.5° and an angular resolution of the pattern of 1°. For the visualization, we present the result for SNRs equal to 20 dB and 30 dB. The locations of the Tx and Rx antenna are presented in Table 1 and are kept the same for all combinations of sampling frequency and SNR. With this parameter set, certain objects in the room are blocked by other objects and, hence, cannot be detected. This is intended to show the potential for improvement and the limitations of the current model and algorithms. However, the total area where objects are identified is almost doubled in comparison with the power map method, where objects are only identified by a peak in the power delay profiles for the main steering vector angular pairs.

Table 1. Location of the transmitter and receiver in the rooms

Axis:		x	y	z
Room A	***Tx***	-3.8	0	1
	Rx	3.8	0	1
Room B	***Tx***	-2.5	-0.5	0.5
	Rx	3	0.5	0.5

Table 2 shows the Chamfer and Hausdorff distances (CD, HD) for different scenarios where λ values are chosen to minimize the CD. The parameter *mean(Power)* refers to the value received as the average power per ellipse in the setting, and it was empirically found that it can help to improve results. Green round points in Figures 10 to 13 are the interactions of the rays with the environment (the first-order reflection or diffraction). They essentially mark the objects that can possibly be 'seen'. The red square points are estimations of the objects using the suggested method. The size of the points corresponds to the relative maximum value. For the estimated (red) points – their size is normalized to the maximum reflective value per scenario. Some of the objects cannot be identified due to limitations of the ray-tracing model. As an example, in Fig. 12 and 13, the object at the very south of the room is blocked and therefore, never is marked with green points. If the rays, after first-order reflection, haven't passed through a small sphere around the receiver – there are no filter coefficients of the channel for that area. To solve this problem, a dynamic scenario, where transmitter or/and receiver change location, can be considered. Another set of rays with new explorable interaction points would be created. Furthermore, it would be beneficial to investigate and discuss the optimal method to merge points generated from several locations of the Tx and Rx in the same room to increase the coverage of all objects.

Figures 10 to 13 show the visual representation with the optimally adjusted regularization parameter λ for each scenario, using a top view of the room. The higher regularization parameter λ is chosen, the more points will fall below the threshold and will not be shown in the final result. Lower SNR makes it harder to distinguish between the interaction and noise. Therefore, if the same value of the regularization parameter λ, is used for all ellipses, more points will be visible in the areas where no objects exist. In certain cases, in Table 2, rather high values for CD and HD are calculated (No. 1 to 4), but the estimation points are still tightly connected with the true interaction points. Still, some of the points were not detected. In such cases, the metrics penalize either the missing point itself or, in some instances, an outlier in the estimated location. In both rooms, areas with transmitter angles close to 90° were not covered, leading to poor estimation results in those regions. If we introduce the 'coverage area' as a parameter and calculate CD and HD for a subset of the true points, the average and worst-case distance errors could be reduced. However, it must be noted that this would only represent a small percentage of the total area that could potentially be observed.

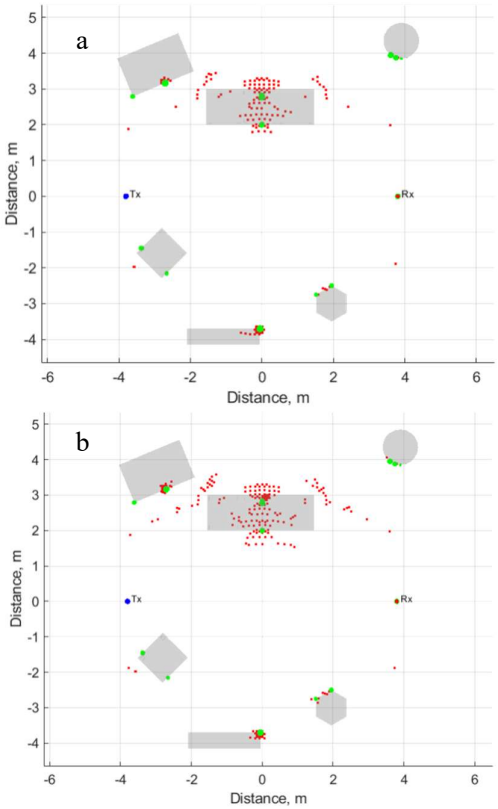

Fig. 10. Visualization point sets for the Room A (a) SNR 20 dB, (b) SNR 30 dB and f_s = 2.19 GHz

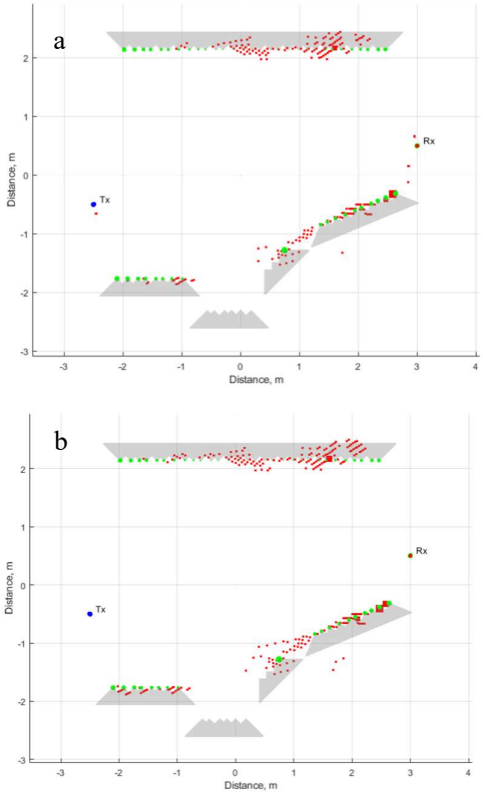

Fig. 12. Visualization points sets for the Room B (a) SNR 20 dB, (b) SNR 30 dB and f_s = 2.19 GHz

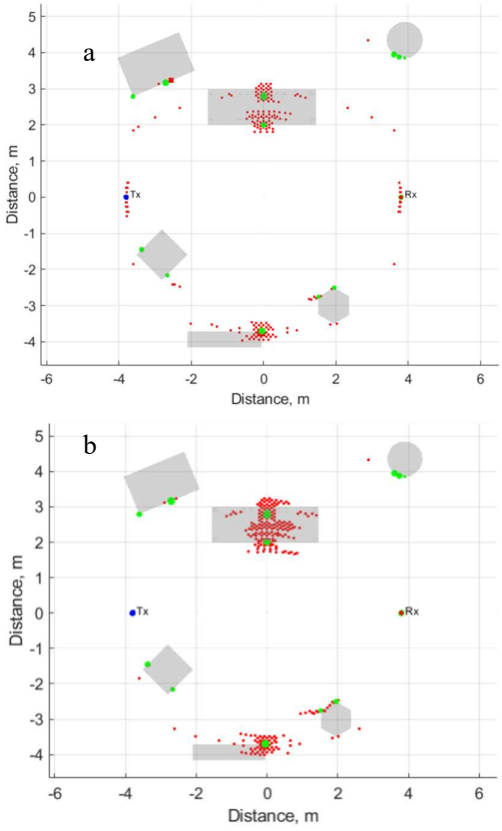

Fig. 11. Visualization point sets for the Room A (a) SNR 20 dB, (b) SNR 30 dB and f_s = 5 GHz

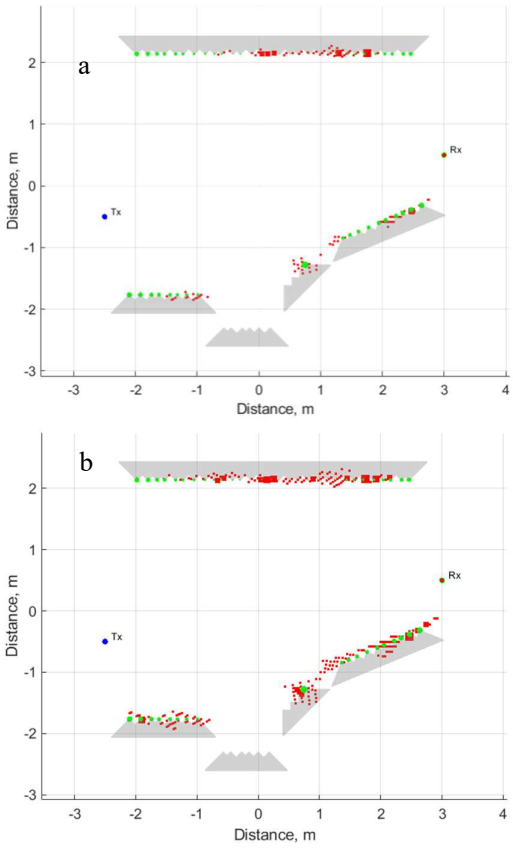

Fig. 13. Visualization points sets for the Room B (a) SNR 20 dB, (b) SNR 30 dB and f_s = 5 GHz

Furthermore, in Table 2, it can be observed that in some cases (Nr. 7 and 8), lower sampling frequency (2.19 GHz) shows a lower value of CD and HD than 5 GHz case. Since the final results and the visualization depend on the chosen value of the regularization parameter λ, there is always a tradeoff between visual impression in comparison with the ground truth (that is achieved quite well) and the possibility to discover further points (therefore, decrease both CD and HD values).

TABLE 2. THE BEST VALUE OF REGULATION PARAMETER WITH THE MINIMIZED CD AND HD PER SCENARIO

№	Scenario	CD, m	HD, m	Regularization parameter λ
1	SNR 30 dB, Room A, f_s = 2.19 GHz	0.739	1.919	0.0035 + 0.0015*mean(Power)
2	SNR 30 dB, Room A, f_s = 5 GHz	0.656	1.487	0.00025 + 0.04*mean(Power)
3	SNR 20 dB, Room A, f_s = 2.19 GHz	0.642	1.895	0.0005 + 0.1*mean(Power)
4	SNR 20 dB, Room A, f_s = 5 GHz	2.499	3.414	0.000365 + 0.017*mean(Power)
5	SNR 30 dB, Room B, f_s = 2.19 GHz	0.041	0.696	0.000587 + 0.002*mean(Power)
6	SNR 30 dB, Room B, f_s = 5 GHz	0.025	0.445	0.000385
7	SNR 20 dB, Room B, f_s = 2.19 GHz	0.11	1.161	0.0006 + 0.0001*mean(Power)
8	SNR 20 dB, Room B, f_s = 5 GHz	0.1529	1.321	0.0075

V CONCLUSIONS AND FUTURE WORK

The usage of the antenna pattern information and corresponding side lobes can significantly improve the object localization for mmWave beamforming ISAC systems. Additionally, it can increase the area coverage if the gain of side lobe rays and the resulting SNR does not fall too low. The SNR value can be improved with adding averaging over multiple measurements and/or simulations to decrease the noise component. Another option for further improvement would be to merge several point clouds of a dynamic scenario, where, for example, the receiver can move along a certain path. This would support the digital twin concept by establishing detailed geometrical models of the environment.

The quality metrics used in this work, such as Chamfer and Hausdorff distances, provide an initial view of performance. A more thorough evaluation with additional or alternative metrics could help highlighting areas for improvement and give a more complete picture in the evaluation of an ISAC system for object localization.

In our future work, we plan to obtain measurement data and verify the results in an anechoic chamber and a real room. This should confirm the option to find not only the main reflection point from the objects (in case of reflection from the flat surfaces in the ray-tracing model), but also the size of the object (in case of scattering and/or diffraction from different rough materials). LASSO as a machine learning method, works quite well in the sparse mmWave scenario modelled with rays. We expect very similar behavior for data coming from real measurement campaigns.

REFERENCES

[1] R. Schneiderman, "LTE Base Stations, Mobile Devices Flood Telecom, Consumer Markets [Special Reports]," IEEE Signal Process. Mag., vol. 29, no. 4, pp. 9–14, Jul. 2012, doi: 10.1109/msp.2012.2186185.

[2] D. Kumar et al., "All Things Considered: An Analysis of IoT Devices on Home Networks," in 28th USENIX Security Symposium, Santa Clara, CA, USA, Aug. 2019, pp. 1169–1185. doi: 10.5555/3361338.3361419.

[3] W. Hong et al., "The Role of Millimeter-Wave Technologies in 5G/6G Wireless Communications," IEEE J. Microw., vol. 1, no. 1, pp. 101–122, Jan. 2021, doi: 10.1109/jmw.2020.3035541.

[4] J. Zhang et al., "A Survey of mmWave-based Human Sensing: Technology, Platform and Applications," IEEE Commun. Surv. Tutor., vol. 25, no. 4, pp. 2052–2087, 2023, doi: 10.1109/COMST.2023.3298300.

[5] T. Konstantinos, C.-A. Katsigiannis, V. Kokkinos, A. Gkamas, C. Bouras, and P. Pougioutas, "Enhancing Spectral Efficiency in 5G MIMO Networks Through Adaptive Beamforming Techniques," in 2024 7th International Conference on Advanced Communication Technologies and Networking (CommNet), Rabat, Morocco: IEEE, Dec. 2024, pp. 1–7. doi: 10.1109/commnet63022.2024.10793345.

[6] I. Ahmed et al., "A Survey on Hybrid Beamforming Techniques in 5G: Architecture and System Model Perspectives," IEEE Commun. Surv. Tutor., vol. 20, no. 4, pp. 3060–3097, 2018, doi: 10.1109/comst.2018.2843719.

[7] Yujie Gu and A. Leshem, "Robust Adaptive Beamforming Based on Interference Covariance Matrix Reconstruction and Steering Vector Estimation," IEEE Trans. Signal Process., vol. 60, no. 7, pp. 3881–3885, Jul. 2012, doi: 10.1109/tsp.2012.2194289.

[8] D. K. Pin Tan et al., "Integrated Sensing and Communication in 6G: Motivations, Use Cases, Requirements, Challenges and Future Directions," in 2021 1st IEEE International Online Symposium on Joint Communications & Sensing (JC&S), Dresden, Germany: IEEE, Feb. 2021, pp. 1–6. doi: 10.1109/jcs52304.2021.9376324.

[9] S. Mihai et al., "Digital Twins: A Survey on Enabling Technologies, Challenges, Trends and Future Prospects," IEEE Commun. Surv. Tutor., vol. 24, no. 4, pp. 2255–2291, 2022, doi: 10.1109/comst.2022.3208773.

[10] N. Maletic et al., "SDR-based 60 GHz Solution for mmWave Applications: Implementation and Evaluation," in 2022 30th Telecommunications Forum (TELFOR), Belgrade, Serbia: IEEE, Nov. 2022, pp. 1–4. doi: 10.1109/telfor56187.2022.9983690.

[11] "Documentation for MATLAB Antenna Toolbox." [Online]. Available: https://ch.mathworks.com/help/antenna/index.html

[12] "Documentation for MATLAB Phased Antenna System Toolbox." [Online]. Available: https://ch.mathworks.com/help/phased/index.html

[13] D. Chu, "Polyphase codes with good periodic correlation properties (Corresp.)," IEEE Trans. Inf. Theory, vol. 18, no. 4, pp. 531–532, Jul. 1972, doi: 10.1109/tit.1972.1054840.

[14] E. Sedunova, N. Maletic, L. Wimmer, D. Cvetkovski, E. Grass, and B. Lankl, "Utilizing Beamsteering at Millimeter Waves for Indoor Object and Room Geometry Detection," in 2021 IEEE 4th 5G World Forum (5GWF), Montreal, QC, Canada: IEEE, Oct. 2021, pp. 340–345. doi: 10.1109/5gwf52925.2021.00066.

[15] E. Sedunova, N. Maletic, D. Cvetkovski, and E. Grass, "Enhanced Object Localization Using a Beamsteering mmWave Communication System," in 2023 6th International Conference on Advanced Communication Technologies and Networking (CommNet), Rabat, Morocco: IEEE, Dec. 2023, pp. 1–6. doi: 10.1109/commnet60167.2023.10365256.

[16] E. Sedunova, N. Maletic, D. Cvetkovski, and E. Grass, "Experimental Object Localization using mmWave Beamforming Communication System," in ITG-Fb. 316: Mobilkommunikation – Technologien und Anwendungen, Osnabrück: VDE, May 2024, pp. 143–148.

[17] "Multicollinearity, LASSO, Ridge Regression, Principal Component Regression," Int. J. Stat. Appl., 2018.

[18] M. Wainwright, R. Tibshirani, and T. Hastie, Statistical Learning with Sparsity The Lasso and Generalizations. 2015.